Ocean Sci., 19, 1579–1593, 2023
https://doi.org/10.5194/os-19-1579-2023
© Author(s) 2023. This work is distributed under
the Creative Commons Attribution 4.0 License.

Ocean Science
Open Access

Impact of surface and subsurface-intensified eddies on sea surface temperature and chlorophyll *a* in the northern Indian Ocean utilizing deep learning

Yingjie Liu and Xiaofeng Li

CAS Key Laboratory of Ocean Circulation and Waves, Institute of Oceanology,
Chinese Academy of Sciences, Qingdao 266071, China

Correspondence: Xiaofeng Li (lixf@qdio.ac.cn)

Received: 29 June 2023 – Discussion started: 5 July 2023
Revised: 25 September 2023 – Accepted: 6 October 2023 – Published: 16 November 2023

Abstract. Mesoscale eddies, including surface-intensified eddies (SEs) and subsurface-intensified eddies (SSEs), significantly influence phytoplankton distribution in the ocean. Nevertheless, due to the sparse in situ data, understanding of the characteristics of SSEs and their influence on chlorophyll *a* (Chl *a*) concentration is still unclear. Consequently, the study utilized a deep learning model to extract SEs and SSEs in the northern Indian Ocean (NIO) from 2000 to 2015, using satellite-derived sea surface height (SSH) and sea surface temperature (SST) data. The analysis revealed that SSEs accounted for 39 % of the total eddies in the NIO, and their SST signatures exhibited opposite behaviour compared to SEs. Furthermore, by integrating ocean colour remote-sensing data, the study investigated the contrasting impacts of SEs and SSEs on Chl *a* concentration in two basins of the NIO, the Arabian Sea (AS) and the Bay of Bengal (BoB), known for their disparate biological productivity. In the AS, SEs induced Chl *a* anomalies that were 2 to 3 times higher than those caused by SSEs. Notably, there were no significant differences in Chl *a* anomalies induced by the same type of eddies between summer and winter. In contrast, the BoB exhibited distinct seasonal variations, where SEs induced slightly higher Chl *a* anomalies than SSEs during the summer, while substantial differences were observed during the winter. Specifically, subsurface-intensified anticyclonic eddies (SSAEs) led to positive Chl *a* anomalies, contrasting the negative anomalies induced by surface-intensified anticyclonic eddies (SAEs) with comparable magnitudes. Moreover, while both subsurface-intensified cyclonic eddies (SSCEs) and surface-intensified cyclonic eddies (SCEs) resulted in positive Chl *a* anomalies during winter in the BoB, the magnitude of SSCEs was only one-third of that induced by SCEs. Besides, subsurface Chl *a* induced by SSAEs (SSCEs) is $\sim 0.1\,\mathrm{mg\,m^{-3}}$ greater (less) than that caused by SAEs (SCEs) in the upper 30 (50) m using Biogeochemical Argo profiles. The distinct Chl *a* between SEs and SSEs can be attributed to their contrasting subsurface structures revealed by Argo profiles. Compared to SAEs (SCEs), SSAEs (SSCEs) enhance (decrease) production via the convex (concave) of the isopycnals that occur around the mixed layer. The study provides a valuable approach to investigating subsurface eddies and contributes to a comprehensive understanding of their influence on chlorophyll concentration.

1 Introduction

Mesoscale eddies widely exist in the global ocean (Chen and Han, 2019; Chen et al., 2021; Chelton et al., 2011b; Faghmous et al., 2015) and significantly influence phytoplankton distribution through several processes, including eddy stirring (Chelton et al., 2011a), eddy trapping (Lehahn et al., 2011), eddy upwelling and downwelling (Gaube et al., 2013), eddy-induced Ekman pumping (Gaube et al., 2014, 2013; Siegel et al., 2011), and eddy strain-induced pumping (Zhang et al., 2019). Previous studies predominantly focused on investigating chlorophyll distribution induced by surface-intensified eddies (SEs), which can be generally classified into surface-intensified anticyclonic eddies (SAEs) and surface-intensified cyclonic eddies (SCEs) based on their rotation direction (Chen et al., 2019). It is important to note

that mesoscale eddies can be further subdivided into distinct categories by the location of their core, where the potential vorticity reaches its maximum. The core can be located in the surface or subsurface layers (Assassi et al., 2016), resulting in SEs or subsurface-intensified eddies (SSEs). SSEs are conjectured to be due to eddy–wind interaction, local adiabatic processes, barotropic and baroclinic instabilities, or topographic influences (Badin et al., 2011; Meunier et al., 2018; Thomas, 2008; McGillicuddy, 2015). Due to the particular lens-like structure of isopycnals, SSEs are an important supplier of nutrients for the euphotic zone and greatly enhance primary production (McGillicuddy et al., 2007; Ledwell et al., 2008; Karstensen et al., 2017). SSEs have been observed in various ocean regions using in situ data, such as the California Undercurrent eddies in the northeastern Pacific (Garfield et al., 1999), the Mediterranean water eddies, and slope water oceanic eddies in the northeastern Atlantic (Bashmachnikov et al., 2013; Paillet et al., 2002). However, the sparse availability of in situ data makes it challenging to determine whether the eddies observed in satellite-derived maps are subsurface-intensified. Therefore, there is still uncertainty for further research regarding the characteristics of SSEs and their impact on chlorophyll concentration.

The surface and interior ocean are highly correlated, and the subsurface signals in the ocean can be reflected at the surface (Klemas and Yan, 2014). The relationship between sea surface height (SSH) and sea surface temperature (SST) within eddies has proven to be an effective index for differentiating between SEs and SSEs using multi-source remote-sensing data (Assassi et al., 2016; Bashmachnikov et al., 2013; Caballero et al., 2008), which has demonstrated successful application across diverse oceanic regions (Wang et al., 2019; Greaser et al., 2020; Trott et al., 2019). However, SST and SSH within eddies are subject to the intricate influence of multiple physical processes, leading to the intricate and nonlinear SST–SSH relationship that traditional statistical methods may not adequately capture. The deep learning (DL) technique has recently demonstrated remarkable capabilities in analyzing and extracting intricate patterns and relationships from multi-source big data (Ham et al., 2019; Lecun et al., 2015; Lu et al., 2019; Su et al., 2015; Jiang et al., 2022; H. Su et al., 2021), enabling a deeper and more comprehensive exploration of the intricate dynamics within SEs and SSEs.

Mesoscale eddies are prominent features in the northern Indian Ocean (NIO) (Zhan et al., 2020; Trott et al., 2019; Chen et al., 2012; Gulakaram et al., 2020; Greaser et al., 2020), which consists of the Bay of Bengal (BoB) and the Arabian Sea (AS), two distinct basins that exhibit substantial differences in terms of their biological productivity. In the NIO, intense southwesterly summer monsoon winds blow between June and September, while relatively weak northeasterly winter winds blow between November and February (Prasad, 2004). Besides, the winds over the AS are stronger than the BoB due to the Findlater Jet during the summer monsoon (Findlater, 1969). The intense summer monsoon makes the AS one of the world's most productive regions (Kumar et al., 2002), with various physical processes contributing to its productivity, such as open ocean upwelling (Brock et al., 1991), wind-driven mixing (Lee et al., 2000), lateral advection (Kumar et al., 2001), and the coastal upwelling along Somalia (Kumar et al., 2002). Conversely, the BoB is regarded as a region with lower biological productivity due to weaker summer monsoon and lower salinity (Kumar et al., 2002; Prasad, 2004). The previous literature mainly investigates the influence of SEs on biological features in the AS and the BoB (Yang et al., 2020; Shafeeque et al., 2021; Smitha et al., 2022). However, both SEs and SSEs were found in the AS (Trott et al., 2019) and the BoB (Greaser et al., 2020; Babu et al., 1991). For example, during the southwest monsoon seasons from 2015 to 2018, Trott et al. (2019) found that 38.6 % of anticyclonic eddies are subsurface-intensified, and 28.5 % of cyclonic eddies are subsurface-intensified in the AS. Considering that the number of SSEs cannot be ignored, further investigations are needed to examine the effects of SSEs on chlorophyll distribution in the NIO.

Therefore, the study proposes a DL-based model to distinguish between SEs and SSEs using satellite-derived altimetry SSH and infrared SST data. Consequently, the study conducts a comparative analysis to assess the differential impacts of SEs and SSEs on chlorophyll concentrations in the NIO. Section 2 introduces the satellite-derived data, in situ data, and methods to distinguish and analyse SEs and SSEs. Section 3 examines and contrasts the spatial characteristics and seasonal variations of SST and chlorophyll anomalies caused by SEs and SSEs in the AS and the BoB. Section 4 of the study focuses on constructing subsurface eddy structures using in situ data to validate the DL-based model's accuracy and explain the differences in chlorophyll distribution caused by SEs and SSEs. In Sect. 5, the study presents its conclusions based on the findings and analysis conducted throughout the research.

2 Data and methods

2.1 Data

2.1.1 Satellite-derived dataset and products

The SSH anomaly (SSHA) dataset is obtained from the European Copernicus Marine Environment Monitoring Service (Pujol et al., 2016). The dataset is derived by combining data from multiple altimeter missions and is available daily. The spatial resolution of the dataset is 0.25°, providing detailed information about the variations in SSH across the study region. A spatial filter with half-power filter cutoffs of 20° longitude by 10° latitude is applied to the SSHA map to facilitate the detection of eddies (Chelton et al., 2011b). The

SST dataset used in the study is the NOAA Optimum Interpolation (OI) SST product from Reynolds et al. (2007). The dataset is available daily and has a spatial resolution of 0.25°. To identify eddy-induced SST anomalies (SSTAs), temporal and spatial filters were applied to the SST field. The temporal filter utilized a band-pass Butterworth window to preserve the temporal signal within 7–90 d. The filter is chosen based on the typical lifetimes of eddies in the NIO, ensuring that the relevant temporal variations associated with eddy dynamics are captured. Meanwhile, the spatial filter employed a moving-average Hann window to retain spatial scales smaller than 600 km. These filters have been shown to provide robust results for obtaining the mesoscale SSTA field (Bôas et al., 2015).

In addition, the ocean-colour-observed chlorophyll *a* (Chl *a*) product is used to evaluate chlorophyll concentrations induced by eddies. The daily Chl *a* dataset of 4 km was produced by the European Space Agency (Maritorena et al., 2010). The Chl *a* measurements were averaged onto the 0.25° grid as the SSHA observations. The unit for Chl *a* concentration is milligrams per cubic metre, and Chl *a* values are firstly log-transformed due to their lognormal distribution. In order to obtain eddy-induced Chl *a* anomalies (Chl-a'), the satellite log-transformed Chl *a* field was first filtered with a 7–90 d Butterworth time filter. The time-filtered Chl *a* field was then anti-log-transformed to get the original units of milligrams per cubic metre for direct comparisons of their results inside eddies (Gaube et al., 2013). Finally, a 600 km high-pass spatial filter was applied to the time-filtered Chl *a* field, generating an eddy-induced Chl-a' field.

2.1.2 In situ data

The study utilizes Argo profiles to construct the subsurface eddy structures. The Argo floats provide temperature and salinity measurements from the sea surface to thousands of metres below, allowing for a comprehensive understanding of subsurface conditions. Besides, the daily climatology of subsurface temperature and salinity values is acquired from the CSIRO Atlas of Regional Seas 2009 (CARS09) product. These climatological values are then subtracted from the Argo profiles, enabling the isolation of anomalies specific to the eddy features. In addition, we used the density-based mixed-layer-depth (MLD) data derived from Argo floats by Holte and Talley (2009) to study the relationship between MLD variations and "abnormal" eddies. MLD data within 1.5 radii (R) of the eddy core on the same day were selected for the study.

Furthermore, to study the differences in vertical chlorophyll distributions between SEs and SSEs, the study utilizes Biogeochemical Argo (BGC-Argo) floats equipped with bio-optical sensors to measure biogeochemical variables. For each BGC-Argo profile, we selected the highest-level data mode (delayed mode), produced later (over 1 year), and required control and validation by a scientific expert. Only profile data flagged as good quality were considered in the study. In addition, we conducted quality control on Chl *a* profiles. First, a three-point moving median filter was applied on each profile to remove spikes (Haëntjens et al., 2020; Bisson et al., 2019). Next, we followed the calibration procedure of Roesler et al. (2017) and Haëntjens et al. (2020) to adjust the Chl *a* data. Finally, quality control was applied to eddy-collocated BGC-Argo floats using the following criteria: (1) Chl *a* data from the upper 10 m were excluded from analyses because large variability and high uncertainty were observed there (J. Su et al., 2021). (2) Besides, each profile must contain at least one data point at a depth of 200 m or greater. This is because the Chl *a* is generally located at the base of the euphotic layer (50–200 m) in the NIO (Mignot et al., 2014). (3) There are more than five observations between 10 and 200 m.

2.2 Methods

2.2.1 DL-based eddy identification model

The study aims to extract SEs and SSEs based on the differences in their thermodynamic structures. Figure 1a illustrates the shape of isopycnal levels for SEs and SSEs, as described in the study by Assassi et al. (2016). SAEs exhibit positive SSHAs and the deepening of isopycnals, resulting in negative sea surface density (SSρ) anomalies. Conversely, SCEs show negative SSHAs and the upward displacement of isopycnals, inducing positive anomalies in SSρ. Therefore, both SCEs and SAEs show negative relationships between SSρ and SSHAs. For SSEs, the scenario is slightly different. Subsurface-intensified AEs (SSAEs) also exhibit positive SSHAs, similar to SAEs. However, the shape of isopycnal levels associated with SSAEs is lens-like, indicating an upward displacement of water above the centre and a downward displacement below it. Similarly, subsurface-intensified CEs (SSCEs) maintain negative SSHAs, as observed in SCEs. However, the isopycnal levels above SSCEs exhibit a depressed shape, indicating a downward displacement of water, while the isopycnals below the SSCEs display a domed shape, indicating an upward displacement. Consequently, the SSρ anomalies within SSEs have the opposite sign compared to SEs, leading to a positive SSρ/SSHA ratio for both SSAEs and SSCEs. Therefore, the sign of SSρ/SSHA can be used as an indicator to distinguish SAEs and SSAEs or SCEs and SSCEs. However, it is important to note that SSρ cannot be directly measured from remote-sensing observations. Instead, at first order, SSρ are primarily influenced by SST variations, which can be observed remotely. Thus, the SSTA–SSHA relationship within eddies can be employed to differentiate between SEs and SSEs, successfully applied in previous studies (Trott et al., 2019; Greaser et al., 2020; Wang et al., 2019).

Accordingly, a DL-based model is developed to distinguish between SEs and SSEs by integrating satellite-derived SSHA and SSTA data mentioned in Sect. 2.1.1. As shown in

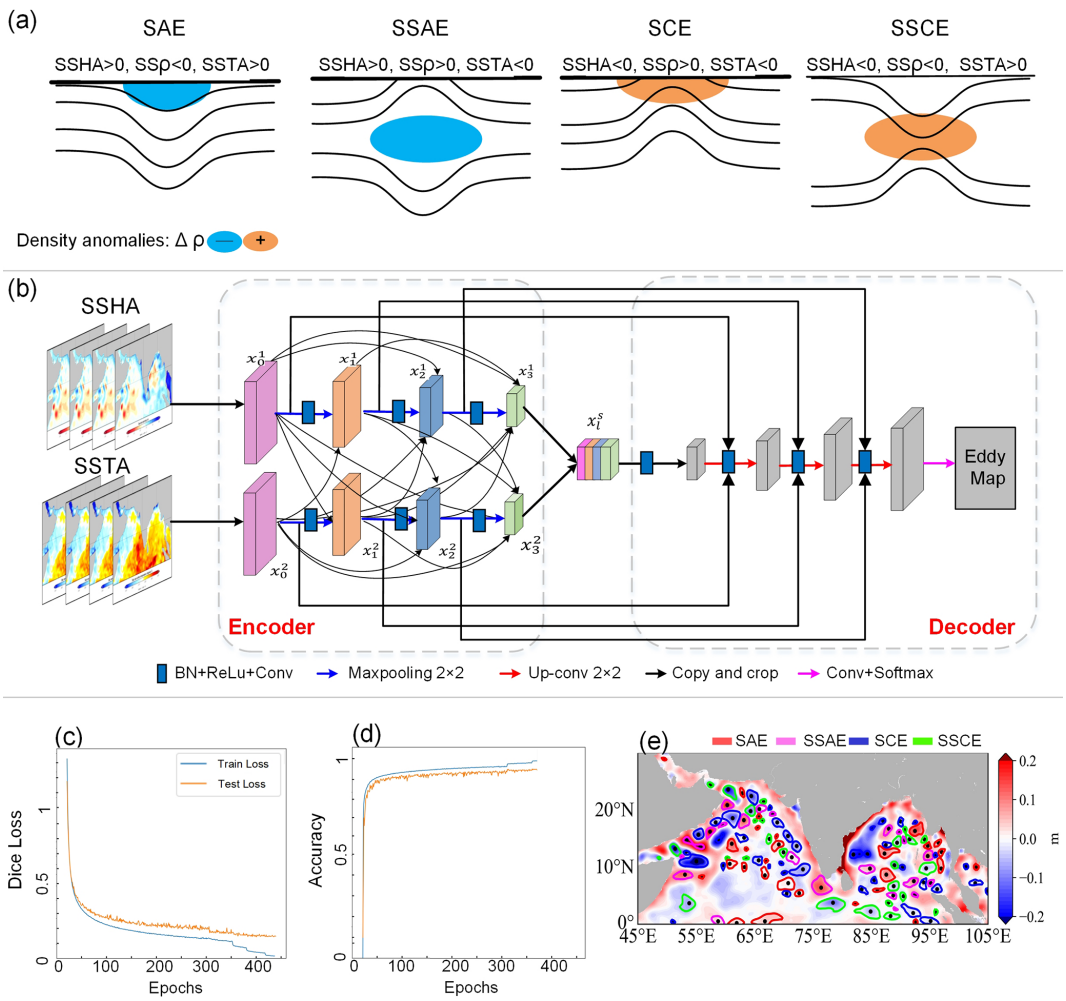

Figure 1. **(a)** Isopycnal displacements, SSHAs, and SSTAs for SAEs, SSAEs, SCEs, and SSCEs. **(b)** Flow chart of the DL-based eddy identification model. Loss **(c)** and accuracy **(d)** curves produced by the DL-based eddy identification model. **(e)** SSCEs, SCEs, SAEs, and SSAEs detected by the DL-based model on 1 December 2005.

Fig. 1b, the DL-based model employs an encoder–decoder architecture (Ronneberger et al., 2015) for feature extraction from SSHA and SSTA data. The encoder–decoder architecture offers several advantages in terms of simplicity, reduced training time, fewer parameters, and lower sample requirements. Consequently, it effectively reduces computational complexity while efficiently extracting features. In the encoder part of the model, convolutions are utilized to extract spatial information from the input image, followed by max pooling to reduce the feature dimensions progressively. In the decoder part, up convolutions are employed to restore object details and spatial information. Besides, features from the corresponding encoder and decoder layers are concatenated to enrich the decoded information. Especially to address the complex nonlinear relationship between SSHAs and SSTAs within mesoscale eddies, a dense connection network (Dolz et al., 2018) is incorporated into the encoder part to facilitate the fusion of remote-sensing SSHA and SSTA data. Unlike traditional convolutional neural networks, where information flows sequentially from one layer to the next, the dense connection network establishes direct connections from any layer to all subsequent layers in a forward manner. The forward propagation is represented by Eq. (1):

$$x_l^s = H_l^s\left(\left[x_{l-1}^1, x_{l-1}^2, x_{l-2}^1, x_{l-2}^2, \ldots, x_0^1, x_0^2\right]\right), \quad (1)$$

where x represents a single network layer, the superscript s denotes the modality of the network layer, and the subscript l indicates the layer number. The function H_l^s represents a composite operation that includes batch normalization (BN), rectified linear unit (ReLU), and convolutional operations. By incorporating dense connections, the DL-based model introduces implicit deep supervision, enhancing learning capabilities and improving information flow and gradient throughout the model. It not only facilitates the extraction of correlated spatiotemporal features of SSHAs and SSTAs at

different scales but also mitigates the issue of gradient vanishing that commonly arises with increasing network depth. Consequently, the proposed model ensures a more efficient and accurate training process.

The DL-based eddy identification model was trained and validated using datasets generated by a traditional SSH-based method (Liu et al., 2016; Chelton et al., 2011b), which extracts AEs and CEs by searching closed SSHA contours. Then, to determine whether an AE is an SAE or SSAE and a CE is an SCE or SSCE, the study calculates the mean SSTA within one radius within eddies. The mean SSTA within SCEs and SSAEs is negative, while it is positive within SAEs and SSCEs. As a result, we obtained the training dataset consisting of 1827 samples from 2000–2004 and the testing dataset consisting of 365 samples from 2005. Each sample contains four kinds of eddies in the NIO: SSCEs, SCEs, SAEs, and SSAEs, with pixels labelled as "1", "2", "3", and "4", respectively. The study utilized dice loss and categorical accuracy to optimize and estimate the DL-based eddy identification model. The dice loss is defined as

$$\text{loss} = 1 - \text{Dicecoef}(P, G). \tag{2}$$

$\text{Dicecoef}(P, G)$, i.e. the dice coefficient, is a popular cost function for segmentation problems in deep learning. Given the predicted segmentation P and the ground truth region G, the dice coefficient is calculated as

$$\text{Dicecoef}(P, G) = \frac{2|P \cap G|}{|P| + |G|}, \tag{3}$$

where $|.|$ is the sum of elements in the area. A good segmentation result is explained by a dice coefficient close to 1. A low dice coefficient (near 0) indicates poor segmentation performance. Categorical accuracy is a metric that calculates the mean accuracy rate across all predictions for multi-class classification problems, which is defined as follows:

$$\text{categorical accuracy} = \frac{\text{TP} + \text{TN}}{\text{TP} + \text{TN} + \text{FP} + \text{FN}}, \tag{4}$$

where TP, TN, FP, and FN represent the number of true positives, true negatives, false positives, and false negatives, respectively. When the model was evaluated on the testing samples, it achieved a loss of approximately 0.12 and an accuracy of around 0.95 (Fig. 1c and d). With a low loss value and a high accuracy rate, the DL-based model demonstrated promising results in accurately identifying and classifying the different types of eddies in the testing samples (Fig. 1e). Considering the resolution and precision of the SSHA product (Pujol et al., 2016), individual eddies with amplitudes ≥ 2 cm and radii ≥ 35 km are selected to avoid the noises from low-energy eddies in the study.

2.2.2 Surface and subsurface composite analysis over eddies

The study conducted a surface composite analysis combining eddy-induced SSTA and Chl-a' data on a normalized grid. The analysis aims to examine the composite patterns of SSTAs and Chl-a' associated with different types of eddies. The eddy-induced SSTA and Chl-a' values within a region twice the radius (R) of each eddy were collected to construct the surface composite analysis. These values were then interpolated onto a normalized circle of the same size, as depicted in Fig. 2a. Next, composite SSTA and Chl-a' maps were generated by averaging the normalized anomaly fields over the eddies of the same type. This process involved grouping the eddies based on their characteristics and calculating the average SSTA and Chl-a' values at each grid point within the normalized circle for each group of eddies.

To analyse the characteristics of eddies' subsurface structures, we select Argo profiles co-located within $1.5R$ from the eddy core to construct the 3D structure of mesoscale eddies. Quality control was first applied to eddy-collocated Argo floats using the following criteria: (1) Only profiles' data flagged as good quality were considered; (2) each Argo profile must contain a data point at a depth of 10 m or less, and at least one data point at a depth of 1000 m or greater; and (3) there are more than 30 observations between 0 and 1000 m. Secondly, temperature and salinity data were interpolated onto a regular 10 m grid ranging from 10 to 1000 m because Argo floats may or may not have observed data at the surface. Thirdly, the Argo profiles were processed by subtracting the CARS09 dataset to obtain temperature and salinity anomalies, specifically within the eddy regions. Moreover, potential density anomalies were calculated by temperature and salinity anomalies according to the International Thermodynamic Equation of Seawater (Mcdougall and Barker, 2011). Subsequently, the temperature and potential density anomalies within $1.5R$ of mesoscale eddies were interpolated into $0.1R \times 0.1R$ grid points up to a horizontal distance of $1.5R$ (Fig. 2b) by the inverse distance weighting interpolation method (Bartier and Keller, 1996) at each depth level (Sun et al., 2019; Yang et al., 2013; Dong et al., 2017). For each grid point, Argo profiles located within the horizontal range of $0.1R$ set the weight value as

$$w_i = e^{-\left(\frac{d}{R}\right)^2}, \tag{5}$$

where d denotes the distance from the profile to the grid point. The final temperature or potential value at each grid point, N_{grid}, is calculated from the profile values N_i as

$$N_{\text{grid}} = \frac{\sum w_i N_i}{\sum w_i}. \tag{6}$$

3 Results

3.1 Case studies of SST and Chl *a* within SEs and SSEs

The study conducts case studies to preliminarily examine characteristics of SSTAs and Chl-a' within SEs and SSEs. As shown in Fig. 3a, the DL-based model detected an SAE

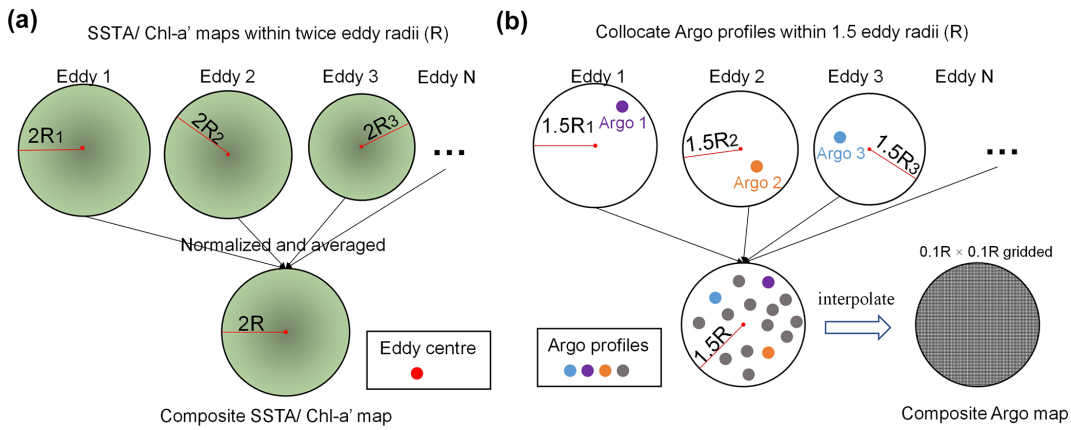

Figure 2. Schematic of composite analysis of SST, Chl *a* **(a)**, and Argo profiles **(b)** for eddies.

and an SCE on the AS's west coast on 2 February 2005. The SAE displays positive signatures in SSTA images, indicating warm water, and negative signatures in Chl-a' images, indicating lower Chl *a* concentrations. In contrast, the SCE shows negative SSTA and positive Chl-a' signatures. These findings are consistent with conventional knowledge, where AEs are generally identified as warm rings with lower Chl *a* concentrations in ocean colour maps, while CEs exhibit the opposite pattern (Gaube et al., 2014; Hsu et al., 2016). Figure 3b shows an example of an SSAE on the east coast of the AS on 13 March 2002. The SSAE is associated with cold water and displays positive Chl-a' signatures, indicating higher Chl *a* concentrations. Similarly, Fig. 3c presents an example of an SSCE in the North Central BoB on 28 November 2014. The SSCE is associated with positive SSTAs, indicating warm water, but exhibits negative Chl-a' values, indicating lower chlorophyll *a* concentrations. The above findings suggest that SSEs exhibit distinct effects on Chl *a* concentrations compared to SEs.

3.2 Spatial distribution of SST and Chl *a* within SEs and SSEs

The study applied the DL-based model to identify SEs and SSEs in the NIO from 2000 to 2015. As a result, 61 095 SAEs, 38 889 SSAEs, 70 596 SCEs, and 46 294 SSCEs are observed. The number represents the aggregate count of eddies of identical type across all eddy snapshots during 2000–2015. Figure 4a–d depict the spatial distribution of eddy concentration, representing eddy numbers of the same type observed within a $1^\circ \times 1^\circ$ grid during 2000–2015. In the NIO, the number of SEs (SAEs and SCEs) accounted for 61 % of the total, while SSEs (SSAEs and SSCEs) constituted 39 %.

The coastal areas of the Arabian Peninsula and the East Indian Coastal Current (EICC) in the BoB exhibited a pronounced abundance and prevalence of SEs and SSEs. These regions are known for their active eddy generation mechanisms, including coastal upwelling, Rossby waves, and barotropic instabilities in the AS (Trott et al., 2018; Zhan et al., 2020), as well as monsoon conversion, EICC instability, and westward Rossby wave energy transmission in the BoB (Somayajulu et al., 2003; Chen et al., 2012; Cheng et al., 2018; Cui et al., 2016). Figure 4e–h display the spatial distributions of eddy-induced SSTAs averaged within a $1^\circ \times 1^\circ$ grid. SAEs and SSCEs exhibit positive SSTA values (Fig. 4e and h), indicating warmer water, while SSAEs and SCEs display negative SSTA values (Fig. 4f and g), indicating cooler water. The distinct SSTA signatures exhibited by these eddies align with the expected patterns associated with SEs and SSEs defined in Sect. 2.2.1.

Figure 5 illustrates the spatial distribution of Chl-a' averaged within a $1^\circ \times 1^\circ$ grid, specifically induced by SEs and SSEs in the NIO during 2000–2015. Chl-a' induced by SAEs (Fig. 5a) exhibits predominantly negative values across most areas of both basins. The western parts of both basins, particularly in the Somali Current (SC) region in the AS, exhibit the lowest concentrations of Chl-a'. It suggests that SAEs are associated with decreased phytoplankton biomass or lower productivity in these regions, whereas Chl-a' induced by SSAEs (Fig. 5b) shows predominantly positive signals in more areas, with a concentration observed along the northeastern coasts of both basins, which indicates that SSAEs are associated with higher productivity in these regions. For SCEs (Fig. 5c), eddy-induced Chl-a' exhibits positive values and a higher concentration along the SC region. In contrast, in most areas, Chl-a' induced by SSCEs (Fig. 5d) is generally insignificant. It shows negative values in the Gulf of Aden and north of the Andaman Sea. It implies that SSCEs may have less effect on primary productivity in these regions than SCEs.

3.3 Seasonal variations of composite SST and Chl *a* within SEs and SSEs

Considering distinct monsoon and productivity backgrounds in the AS and the BoB regions, we conducted a composite

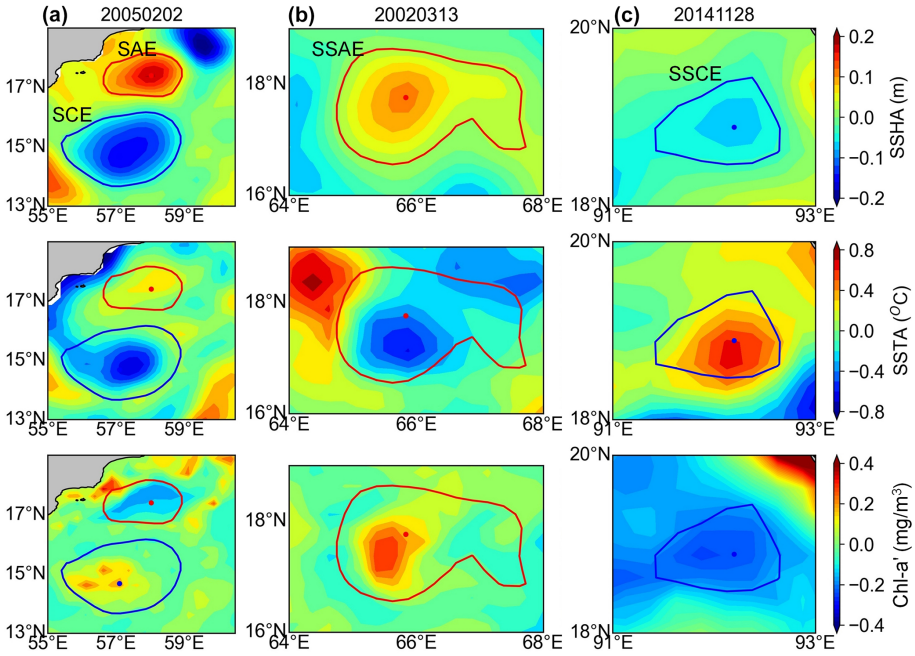

Figure 3. Case study of eddy imprints on SSHAs, SSTAs, and Chl-a' maps for an SAE and an SCE **(a)**, an SSAE **(b)**, and an SSCE **(c)**. Red and blue lines denote eddy edges.

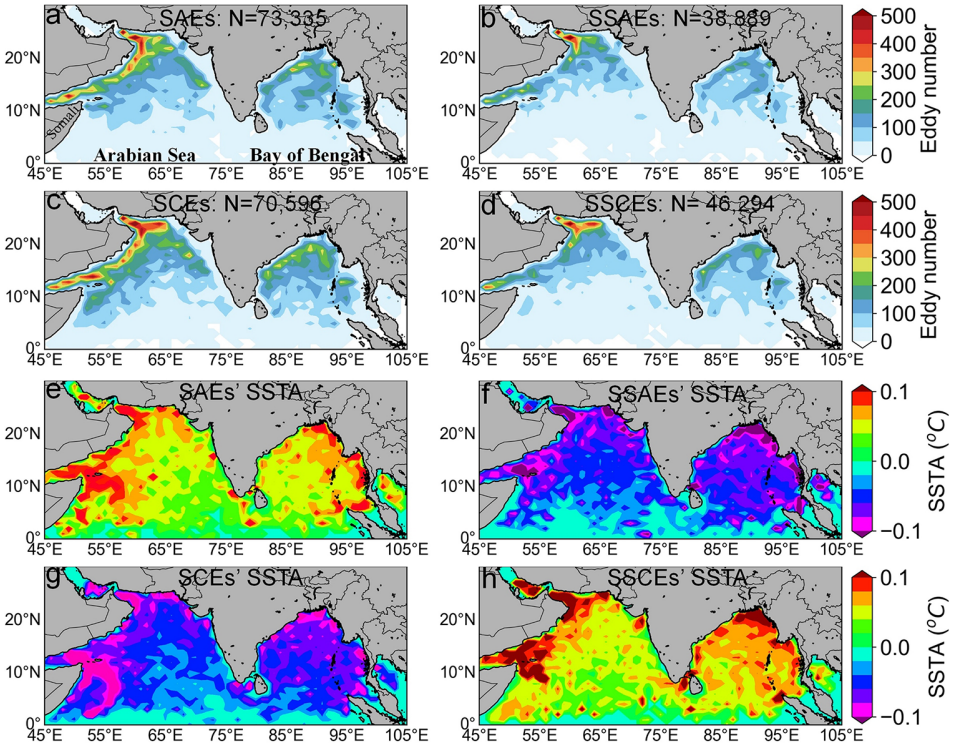

Figure 4. The spatial distribution of eddy concentration **(a–d)** and SSTAs **(e–h)** within SAEs, SSAEs, SCEs, and SSCEs. N is the sum of eddies of the same kind observed in the NIO during 2000–2015.

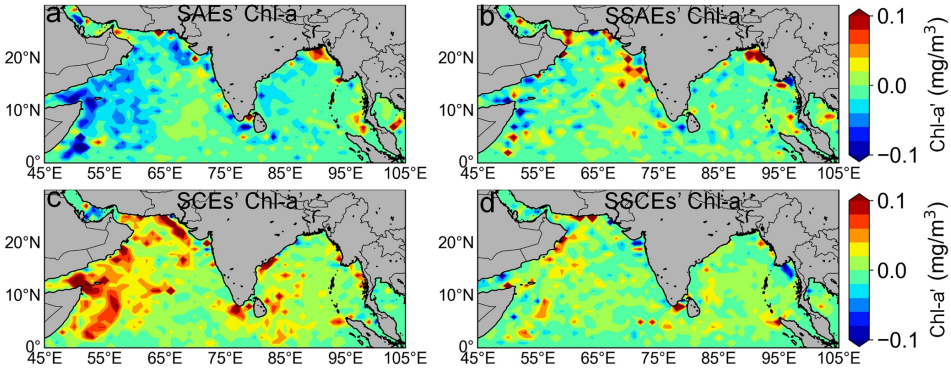

Figure 5. Spatial distribution of eddy-induced Chl-a' for SAEs **(a)**, SSAEs **(b)**, SCEs **(c)**, and SSCEs **(d)** in the NIO during 2000–2015.

analysis of SSTAs and Chl-a' within SAEs, SSAEs, SCEs, and SSCEs in summer and winter monsoons for both basins. Figure 6 shows composite SSTAs over SEs and SSEs in the AS and the BoB during summer and winter monsoons. In both basins, composite SSTAs over the SEs and SSEs exhibit similar monopole patterns with opposite signals. Specifically, the composite SSTA signals for SAEs were positive, while those for SCEs were negative. Conversely, the signals for SSAEs were positive, and SSCEs displayed negative SSTA patterns. Despite the opposite SSTA signals between the SEs and SSEs, their magnitudes were comparable within the same season, indicating that the inversed SSTA signal within SSEs should not be overlooked.

In addition, eddy-induced SSTAs over both SEs and SSEs are more pronounced during summer compared to winter in the AS (Fig. 6a–h). Table 1 shows that composite SSTA extrema within SEs and SSEs during summer are at least 1.6 times higher than those observed during winter. The seasonal variation in the intensity of monsoon winds is suggested to influence the impact of eddy-induced SSTAs in the AS throughout the year. The intensified southwesterly winds during the summer monsoon contribute to enhanced upwelling and mixing processes, leading to greater changes in SSTAs induced by eddies. In contrast, the weaker northeasterly winds during the winter monsoon are associated with reduced upwelling and mixing, leading to relatively less pronounced eddy-induced SSTAs. However, composite SSTAs over the SEs and SSEs did not exhibit a significant seasonal variation in the BoB. The intensities of eddy-induced SSTAs were slightly larger during the summer monsoon than in winter, with a difference of 0.01 °C (Table 1). The observed slight difference in intensity of composite eddy-induced SSTAs between the BoB and the AS can be primarily attributed to the seasonal variations in monsoon winds. The BoB exhibits a less pronounced seasonal variation in monsoon winds than the AS. During the summer monsoon, the AS experiences stronger winds than the BoB, while both basins encounter relatively weaker winds during the winter monsoon. The divergence in wind strength contributes significantly to the distinct intensity of eddy-induced SSTAs between the two basins.

Despite the opposing signals of SSTAs induced by SEs and SSEs, they generally exhibit a consistent signal in terms of Chl-a' (Fig. 7). In the AS, composite Chl-a' shows dipole patterns with positive signals for SAEs and SSAEs and negative signals for SCEs and SSCEs (Fig. 7a–h). Although the Chl-a' signals within the SEs and SSEs exhibit similar patterns, their magnitudes significantly differ. According to the data presented in Table 1, the Chl-a' values induced by SAEs during summer and winter are -0.040 and $-0.049\,\mathrm{mg\,m^{-3}}$, respectively. Conversely, the Chl-a' values induced by SSAEs during summer and winter are -0.017 and $-0.012\,\mathrm{mg\,m^{-3}}$, respectively. This indicates that the Chl a concentration within SAEs is notably lower than SSAEs, with approximately half of the concentration observed in the latter. On the other hand, the Chl a concentration within SCEs is 2 to 3 times higher compared to SSCEs. Specifically, the Chl-a' induced by SCEs during summer and winter is 0.076 and $0.084\,\mathrm{mg\,m^{-3}}$, respectively, whereas the Chl-a' induced by SSCEs during summer and winter is 0.018 and $0.039\,\mathrm{mg\,m^{-3}}$, respectively. Notably, Chl-a' intensities over both SEs and SSEs in the AS demonstrate a relatively consistent pattern between the summer and winter monsoons, with no significant variation observed. Winter productivity in the AS has been suggested to be comparable to, or occasionally even surpass, that of the summer (Piontkovski et al., 2011). The enhanced productivity during winter is attributed to the convective winter mixing, which facilitates the upward transport of nutrients to the surface layer (Banse and English, 2000).

However, significant seasonal variations are observed in the impact of SEs and SSEs on Chl a concentration in the BoB (Fig. 7i–p). During the summer monsoon, eddy-induced Chl-a' values over the SEs and SSEs exhibit similar patterns (Fig. 7i–l), with slight differences in magnitudes. As shown in Table 1, the Chl-a' values induced by SAEs and SSAEs are -0.029 and $-0.021\,\mathrm{mg\,m^{-3}}$, indicating a decrease in chlorophyll concentration compared to the surrounding ar-

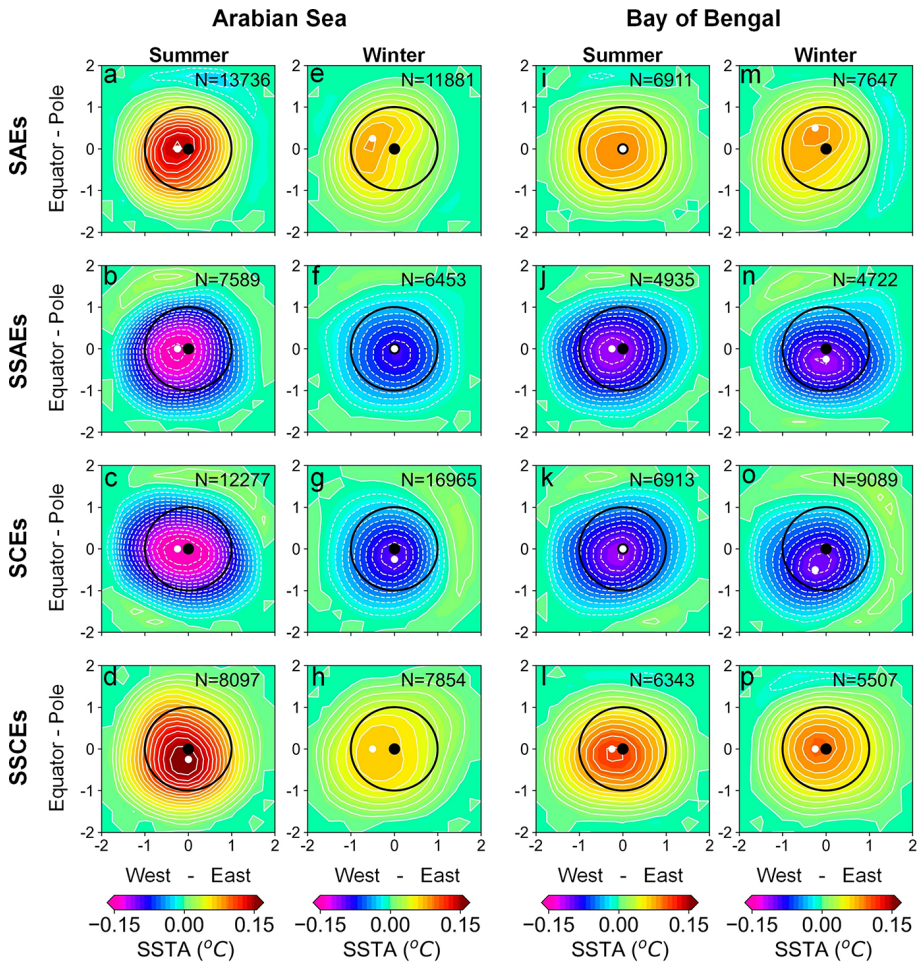

Figure 6. Composite SSTAs over SAEs, SSAEs, SCEs, and SSCEs in the AS **(a–d, i–l)** and BoB **(e–h, m–p)**, respectively. Black points denote eddy centres, while white points represent SSTA extremum locations. N is the sum of eddies of the same kind during 2000–2015.

Table 1. Composite extremum values ±1 confidence interval (CI) for SSTAs and Chl-a' over four kinds of eddies. The CI was computed at the location of SSTA–Chl-a' extrema in composite maps.

		AS		BoB	
		Summer	Winter	Summer	Winter
SSTA (°C)	SAEs	0.14 ± 0.004	0.08 ± 0.002	0.09 ± 0.003	0.08 ± 0.003
	SSAEs	-0.15 ± 0.004	-0.09 ± 0.002	-0.12 ± 0.004	-0.11 ± 0.003
	SCEs	-0.16 ± 0.004	-0.10 ± 0.002	-0.11 ± 0.004	-0.10 ± 0.003
	SSCEs	0.16 ± 0.004	0.07 ± 0.002	0.11 ± 0.003	0.10 ± 0.003
Chl-a' ($\mathrm{mg\,m^{-3}}$)	SAEs	-0.040 ± 0.004	-0.049 ± 0.005	-0.029 ± 0.004	-0.018 ± 0.002
	SSAEs	-0.017 ± 0.004	-0.012 ± 0.002	-0.021 ± 0.003	0.027 ± 0.004
	SCEs	0.076 ± 0.007	0.084 ± 0.005	0.021 ± 0.006	0.033 ± 0.004
	SSCEs	0.018 ± 0.003	0.039 ± 0.007	0.018 ± 0.005	0.010 ± 0.003

eas. On the other hand, SCEs and SSCEs exhibit positive Chl-a' values of 0.021 and 0.018 $\mathrm{mg\,m^{-3}}$, respectively, indicating an increase in chlorophyll concentration. During the winter monsoon, composite Chl-a' values induced by SEs and SSEs exhibit distinct patterns (Fig. 7m–p). Specifically, SAEs exhibit a predominant presence of negative Chl-a' values, with a minimum concentration of $-0.018\,\mathrm{mg\,m^{-3}}$. In contrast, SSAEs are characterized by positive Chl-a' values, reaching a maximum concentration of $0.027\,\mathrm{mg\,m^{-3}}$. Besides, SCEs predominantly exhibit positive Chl-a' values,

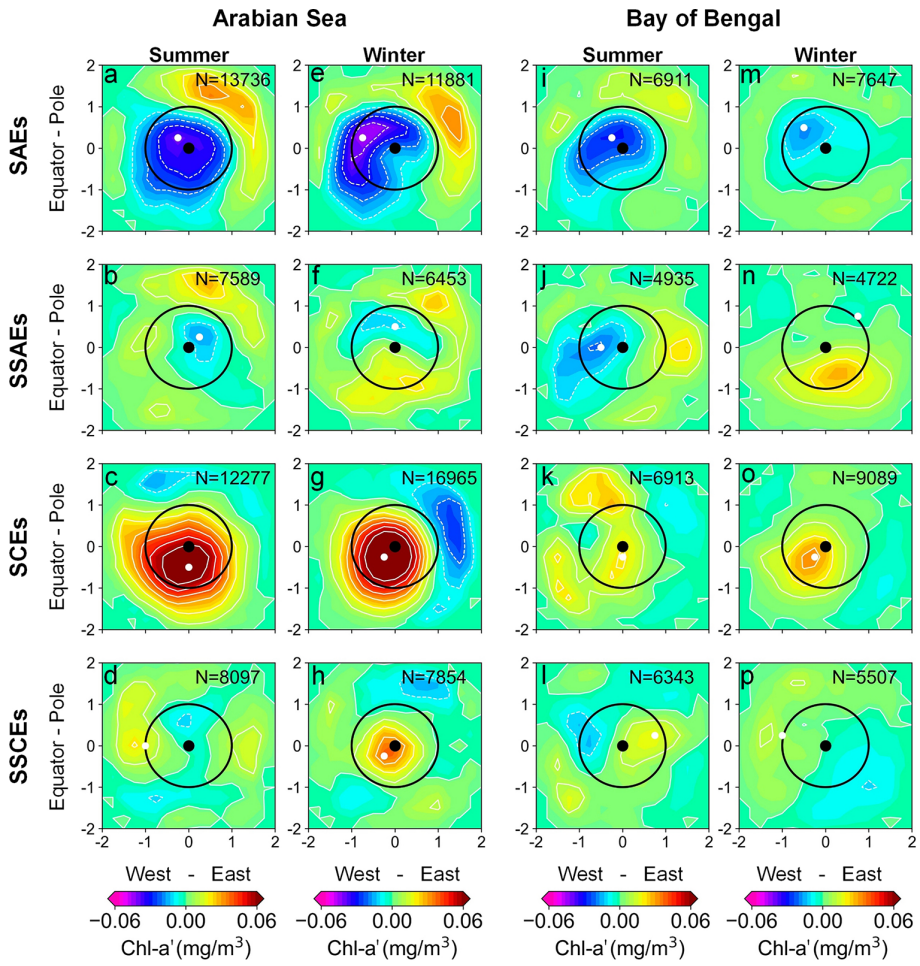

Figure 7. Composite Chl-a' over SAEs, SSAEs, SCEs, and SSCEs in the AS **(a–d, i–l)** and BoB **(e–h, m–p)**, respectively. Black points denote eddy centres, while white points represent Chl-a' extremum locations. N is the sum of eddies of the same kind during 2000–2015.

with a maximum concentration of 0.033 mg m^{-3}, which is approximately 3 times higher than that induced by SSCEs. Additionally, the concentration of eddy-induced Chl-a' in the BoB was considerably lower than in the AS. The lower Chl a concentration within eddies in the BoB is attributed to weakened vertical mixing resulting from freshwater-induced stratification and relatively weaker winds (Prasanna Kumar et al., 2002).

4 Discussion

Relying solely on the SSHA–SSTA relationship may lead to potential misidentification of SSEs due to various sources of errors (Assassi et al., 2016). For example, it is challenging when dealing with eddies exhibiting multicore structures of similar strength, making it difficult to determine the location of the most intense core accurately. Besides, in regions where salinity plays a significant role in stratification, variations of SSρ may not be dominated by SST variations at first order. In order to validate the accuracy and robustness of the DL-based eddy identification model, the study employs quality-controlled Argo profiles to construct subsurface eddy structures for both SEs and SSEs in the AS and the BoB. During 2000–2015, the numbers of Argo profiles within SAEs, SSAEs, SCEs, and SSCEs were as follows: 2777, 1028, 2336, and 1747 profiles in the AS and 778, 374, 648, and 424 profiles in the BoB, respectively.

Figure 8 provides insights into the subsurface temperature anomalies within SEs (SAEs and SCEs) and SSEs (SSAEs and SSCEs) in the AS and the BoB. In the AS, SAEs and SCEs exhibit positive and negative temperature anomalies throughout the structure, with maximum and minimum temperature anomalies at approximately 100 m (Fig. 8a and c). Conversely, SSAEs and SSCEs display negative and positive temperature anomalies approximately within the MLD at around 30 m, contrasting with their subsurface layers (Fig. 8b and d). Similar differences in the subsurface temperature structure between SEs and SSEs are also observed in the BoB (Fig. 8e and h). Specifically, the SAEs (SCEs) showed positive (negative) temperature anomalies throughout the water

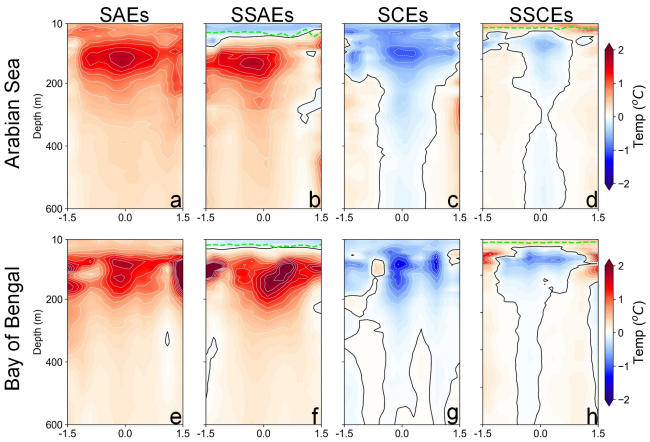

Figure 8. Composite zonal sections of the vertical temperature structure within SAEs, SSAEs, SCEs, and SSCEs in the AS **(a–d)** and the BoB **(e–h)** during 2000–2015. Black lines denote contours in 0 °C. The dashed lime lines in SSAEs and SSCEs denote the MLD.

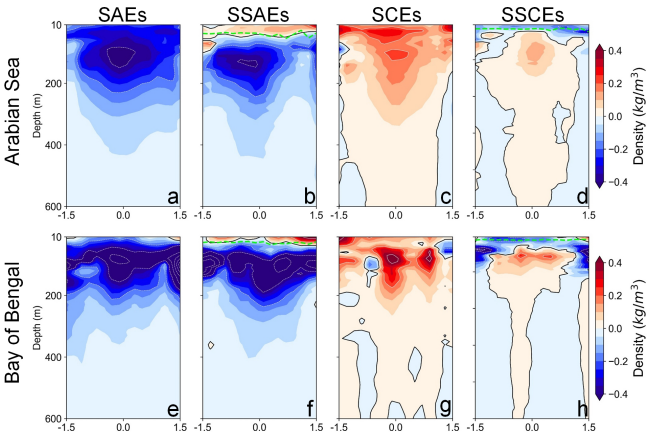

Figure 9. Composite zonal sections of the vertical potential density structure within SAEs, SSAEs, SCEs, and SSCEs in the AS **(a–d)** and the BoB **(e–h)** from 2000–2015. Black lines denote potential density in 0 kg m^{-3}. The dashed lime lines in SSAEs and SSCEs denote the MLD.

column, while the SSAEs (SSCEs) displayed a small cap of cold (warm) water within the MLD.

Furthermore, the study constructs vertical structures of potential density within the eddies (Fig. 9) to determine whether the isopycnal displacements of SEs and SSEs align with the definition proposed by Assassi et al. (2016). In the AS, SAEs and SCEs exhibit negative and positive potential density anomalies throughout the structure, respectively (Fig. 9a and c). However, SSAEs and SSCEs show a small cap of positive and negative potential density anomalies within the MLD, contrasting with their subsurface layers (Fig. 9b and d). Similar patterns are observed in the BoB, where SSAEs and SSCEs display positive and negative potential density anomalies within the MLD, respectively

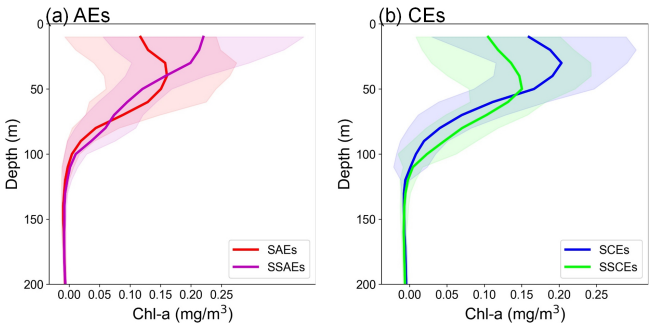

Figure 10. Mean (solid line) and standard deviation (shadow) values of BGC-Argo Chl *a* profiles for SAEs and SSAEs **(a)** and SCEs and SSCEs **(b)** in the northern Indian Ocean during 2000–2015.

(Fig. 9f). Thus, SSAEs generally exhibit positive potential density anomalies in the near-surface layer, which can be attributed to the upward displacement of isopycnals. In contrast, SSCEs show negative potential density anomalies due to downward displacement. These findings align well with the schematic diagram of isopycnal displacements of SEs and SSEs depicted in Fig. 1a. By reconstructing the subsurface structure of eddies, the study confirms the accuracy of the DL-based model in distinguishing between SEs and SSEs. Besides, Figs. 8 and 9 reveal that the difference in the subsurface structure between SEs and SSEs is largely confined to the MLD. Such a result indicates that the formation of SSEs is dominated by eddy–wind interaction (McGillicuddy, 2015), which leads to lens-shaped disturbances in the thermocline. The relative motion between surface winds and eddy surface currents leads to anomalous Ekman upwelling (downwelling) within AEs (CEs), which can induce doming (depressing) of the upper-ocean density surfaces inside AEs (CEs) (Gaube et al., 2015).

Additionally, the study reveals subsurface Chl *a* characteristics of SEs and SSEs using eddy-collocated BGC-Argo floats. In the NIO, spanning the years 2000 to 2015, we identified a total of 30 BGC-Argo profiles located within 1.5R of AEs (CEs), which met our rigorous quality control criteria, as detailed in Sect. 2.1.2. Among these profiles, 18 (12) BGC-Argo profiles were found within 1.5R of SAEs (SSAEs), while 32 (13) BGC-Argo profiles were found within 1.5R of SCEs (SSCEs). Despite the relatively limited number of BGC-Argo profiles, our analysis unmistakably reveals discernible distinctions in the Chl *a* profiles between SAEs and SSAEs, as well as SCEs and SSCEs. As shown in Fig. 10, the variations in Chl *a* induced by eddies are predominantly concentrated within the upper 100 m of the water column. The observation aligns with previous research findings that suggest that Chl *a* tends to be concentrated at the base of the euphotic layer, typically spanning depths of 50 to 200 m in the NIO (Mignot et al., 2014). Furthermore, it is worth noting that Chl *a* levels induced by SSAEs exhibit a substantial increase, approximately 0.1 mg m^{-3}, compared to those

induced by SAEs within the upper 30 m (Fig. 10a). In contrast, the Chl *a* concentrations induced by SSCEs are notably lower, approximately 0.1 mg m^{-3}, in comparison to SCEs within the upper 50 m (Fig. 10b). These disparities can be attributed to distinct displacements of isopycnals between SEs and SSEs. The convex of isopycnals within SSAEs leads to the ascent of deeper water to the surface layer. This process facilitates the vertical transport of nutrients, promoting enhanced biological productivity and higher concentrations of Chl *a* within SSAEs than SAEs. The vertical movement of water masses and the associated nutrient supply contribute to the favourable conditions for phytoplankton growth and the accumulation of Chl *a* in SSAEs. Similarly, the concave of the isopycnals within SSCEs leads to the subduction of surface water, resulting in lower Chl *a* concentrations compared to SCEs.

5 Conclusions

The study proposes a DL-based model that integrates satellite-derived SSH and SST data to accurately distinguish between SEs and SSEs in the NIO during 2000–2015. In the NIO, the number of SEs (SAEs and SCEs) accounted for 61 % of the total, while SSEs (SSAEs and SSCEs) constituted 39 %. SAEs and SCEs exhibit positive and negative SSTAs, contrary to SSAEs and SSCEs, respectively. In addition, SEs and SSEs show significant differences in spatial characteristics and composite patterns of eddy-induced Chl *a*. On the one hand, SAEs (SCEs) induce negative (positive) anomalies in Chl *a* concentration, with the most significant effects observed in the Somali Current region. However, SSAEs cause positive Chl *a* anomalies along the northeastern coast of both basins, while SSCEs lead to negative Chl *a* anomalies in the Gulf of Aden and the northern part of the Andaman Sea. On the other hand, composite Chl *a* within SAEs is considerably lower compared to SSAEs, which is about 2 times lower in the latter. In contrast, the Chl *a* concentration in SCEs is 2 or 3 times higher than in the SSCEs. Moreover, using BGC-Argo profiles, SEs and SSEs show significant differences in subsurface Chl *a* distribution. Chl *a* induced by SSAEs is ~ 0.1 mg m^{-3} greater than that caused by SAEs in the upper 30 m, while Chl *a* induced by SSCEs is ~ 0.1 mg m^{-3} less than that caused by SCEs in the upper 50 m.

The distinct subsurface structures between SEs and SSEs provide insight into the contrasting impacts on Chl *a* distribution. SAEs and SCEs exhibit negative and positive potential density anomalies throughout the structure. However, SSAEs exhibit positive potential density anomalies within the MLD, which can be attributed to the upward displacement of isopycnals. The upward movement facilitated the transport of deeper water to the surface layer, inducing higher Chl *a* concentrations within SSAEs. Besides, SSCEs show negative potential density anomalies above the MLD due to the downward displacement of isopycnals, leading to lower Chl *a* concentrations than SCEs. In conclusion, the study demonstrates the effectiveness of the DL-based model in distinguishing between SEs and SSEs by fusing remote-sensing SSH and SST data. By applying the model, the study enhances the comprehension of the impacts of SSEs on Chl *a* distribution and contributes to a deeper understanding of the complex interactions between eddy dynamics and biogeochemical processes.

Code and data availability. All data used in the analysis are available in public repositories. The SSHA dataset is available at https://doi.org/10.48670/moi-00148. The OI SST product can be downloaded from https://psl.noaa.gov/data/gridded/data.noaa.oisst.v2.highres.html (last access: 14 November 2023). The Chl *a* data were downloaded from http://www.globcolour.info (last access: 14 November 2023). Argo data can be downloaded from http://www.coriolis.eu.org (last access: 14 November 2023). CARS2009 data were obtained from http://www.marine.csiro.au/~dunn/cars2009/ (last access: 14 November 2023). BGC-Argo data can be downloaded from https://dataselection.euro-argo.eu/ (last access: 14 November 2023). The mixed-layer-depth data can be downloaded from http://mixedlayer.ucsd.edu/ (last access: 14 November 2023). The code of the DL-based model is available at https://doi.org/10.6084/m9.figshare.23599683 (Liu and Li, 2023a), and the dataset of eddy-induced chlorophyll *a* used in this paper can be downloaded from https://doi.org/10.6084/m9.figshare.23599473 (Liu and Li, 2023b).

Author contributions. YL and XL: writing, analysis, and revision. Both authors provided feedback on the analysis and interpretation of results and contributed to reviewing and editing the manuscript. Both authors have read and agreed to the published version of the manuscript.

Competing interests. The contact author has declared that neither of the authors has any competing interests.

Disclaimer. Publisher's note: Copernicus Publications remains neutral with regard to jurisdictional claims made in the text, published maps, institutional affiliations, or any other geographical representation in this paper. While Copernicus Publications makes every effort to include appropriate place names, the final responsibility lies with the authors.

Special issue statement. This article is part of the special issue "Special Issue for the 54th International Liège Colloquium on Machine Learning and Data Analysis in Oceanography". It is not associated with a conference.

Acknowledgements. The authors would like to thank the two anonymous reviewers and Ana Ruescas for their detailed and helpful comments.

Financial support. This research has been supported by the Qingdao National Laboratory for Marine Science and Technology through the special fund of Shandong Province (grand no. LSKJ202204302), the Natural Science Foundation of Shandong Province (grand no. ZR2020MD083), the National Natural Science Foundation of China (grand nos. U2006211 and 42306194), the Strategic Priority Research Program of the Chinese Academy of Sciences (grand nos. XDA19060101 and XDB42000000), major scientific and technological innovation projects of Shandong Province (grand no. 2019JZZY010102), and the CAS programme (grand no. Y9KY04101L).

Review statement. This paper was edited by Ana Ruescas and reviewed by two anonymous referees.

References

Assassi, C., Morel, Y., Vandermeirsch, F., Chaigneau, A., Pegliasco, C., Morrow, R., Colas, F., Fleury, S., Carton, X., and Klein, P.: An index to distinguish surface- and subsurface-intensified vortices from surface observations, J. Phys. Oceanogr., 46, 2529–2552, https://doi.org/10.1175/JPO-D-15-0122.1, 2016.

Babu, M. T., Kumar, S. P., and Rao, D. P.: A subsurface cyclonic eddy in the Bay of Bengal, J. Mar. Res., 49, 403–410, 1991.

Badin, G., Tandon, A., and Mahadevan, A.: Lateral mixing in the pycnocline by baroclinic mixed layer eddies, J. Phys. Oceanogr., 41, 2080–2101, https://doi.org/10.1175/JPO-D-11-05.1, 2011.

Banse, K. and English, D.: Geographical differences in seasonality of CZCS-derived phytoplankton pigment in the Arabian Sea for 1978–1986, Deep-Sea Res. Pt. II, 47, 1623–1677, https://doi.org/10.1016/S0967-0645(99)00157-5, 2000.

Bartier, P. M. and Keller, C. P.: Multivariate interpolation to incorporate thematic surface data using inverse distance weighting (IDW), Comput. Geosci., 22, 795–799, https://doi.org/10.1016/0098-3004(96)00021-0, 1996.

Bashmachnikov, I., Boutov, D., and Dias, J.: Manifestation of two meddies in altimetry and sea-surface temperature, Ocean Sci., 9, 249–259, https://doi.org/10.5194/os-9-249-2013, 2013.

Bisson, K., Boss, E., Westberry, T., and Behrenfeld, M.: Evaluating satellite estimates of particulate backscatter in the global open ocean using autonomous profiling floats, Opt. Express, 27, 30191–30203, https://doi.org/10.1364/OE.27.030191, 2019.

Bôas, A. B. V., Sato, O. T., Chaigneau, A., and Castelão, G. P.: The signature of mesoscale eddies on the air-sea turbulent heat fluxes in the South Atlantic Ocean, Geophys. Res. Lett., 42, 1856–1862, https://doi.org/10.1002/2015GL063105, 2015.

Brock, J. C., McClain, C. R., Luther, M. E., and Hay, W. W.: The phytoplankton bloom in the northwestern Arabian Sea during the southwest monsoon of 1979, J. Geophys. Res.-Oceans, 96, 20623–20642, https://doi.org/10.1029/91JC01711, 1991.

Caballero, A., Pascual, A., Dibarboure, G., and Espino, M.: Sea level and Eddy Kinetic Energy variability in the Bay of Biscay, inferred from satellite altimeter data, J. Marine Syst., 72, 116–134, https://doi.org/10.1016/j.jmarsys.2007.03.011, 2008.

Chelton, D. B., Gaube, P., Schlax, M. G., Early, J. J., and Samelson, R. M.: The influence of nonlinear mesoscale eddies on near-surface oceanic chlorophyll, Science, 334, 328–332, https://doi.org/10.1126/science.1208897, 2011a.

Chelton, D. B., Schlax, M. G., and Samelson, R. M.: Global observations of nonlinear mesoscale eddies, Prog. Oceanogr., 91, 167–216, https://doi.org/10.1016/j.pocean.2011.01.002, 2011b.

Chen, G. and Han, G.: Contrasting short–lived with long–lived mesoscale eddies in the global ocean, J. Geophys. Res.-Oceans, 124, 3149–3167, https://doi.org/10.1029/2019JC014983, 2019.

Chen, G., Wang, D., and Hou, Y.: The features and interannual variability mechanism of mesoscale eddies in the Bay of Bengal, Cont. Shelf Res., 47, 178–185, https://doi.org/10.1016/j.csr.2012.07.011, 2012.

Chen, G., Han, G., and Yang, X.: On the intrinsic shape of oceanic eddies derived from satellite altimetry, Remote Sens. Environ., 228, 75–89, https://doi.org/10.1016/j.rse.2019.04.011, 2019.

Chen, G., Yang, J., and Han, G.: Eddy morphology: Egg-like shape, overall spinning, and oceanographic implications, Remote Sens. Environ., 257, 112348, https://doi.org/10.1016/j.rse.2021.112348, 2021.

Cheng, X., McCreary, J. P., Qiu, B., Qi, Y., Du, Y., and Chen, X.: Dynamics of Eddy Generation in the Central Bay of Bengal, J. Geophys. Res.-Oceans, 123, 6861–6875, https://doi.org/10.1029/2018jc014100, 2018.

Cui, W., Yang, J., and Ma, Y.: A statistical analysis of mesoscale eddies in the Bay of Bengal from 22 year altimetry data, Acta Oceanol. Sin., 35, 16–27, https://doi.org/10.1007/s13131-016-0945-3, 2016.

Dolz, J., Gopinath, K., Yuan, J., Lombaert, H., Desrosiers, C., and Ayed, I. B.: HyperDense-Net: A hyper-densely connected CNN for multi-modal image segmentation, IEEE T. Med. Imaging, 38, 1116–1126, https://doi.org/10.1109/TMI.2018.2878669, 2018.

Dong, D., Brandt, P., Chang, P., Schütte, F., Yang, X., Yan, J., and Zeng, J.: Mesoscale Eddies in the Northwestern Pacific Ocean: Three-Dimensional Eddy Structures and Heat/Salt Transports, J. Geophys. Res.-Oceans, 122, 9795–9813, https://doi.org/10.1002/2017jc013303, 2017.

Faghmous, J. H., Frenger, I., Yao, Y., Warmka, R., Lindell, A., and Kumar, V.: A daily global mesoscale ocean eddy dataset from satellite altimetry, Scientific Data, 2, 150028, https://doi.org/10.1038/sdata.2015.28, 2015.

Findlater, J.: A major low-level air current near the Indian Ocean during the northern summer, Q. J. Roy. Meteor. Soc., 95, 362–380, https://doi.org/10.1002/qj.49709540409, 1969.

Garfield, N., Collins, C. A., Paquette, R. G., and Carter, E.: Lagrangian exploration of the California Undercurrent, 1992–95, J. Phys. Oceanogr., 29, 560–583, 1999.

Gaube, P., Chelton, D. B., Strutton, P. G., and Behrenfeld, M. J.: Satellite observations of chlorophyll, phytoplankton biomass, and Ekman pumping in nonlinear mesoscale eddies, J. Geophys. Res.-Oceans, 118, 6349–6370, https://doi.org/10.1002/2013jc009027, 2013.

Gaube, P., McGillicuddy, D. J., Chelton, D. B., Behrenfeld, M. J., and Strutton, P. G.: Regional variations in the influence of mesoscale eddies on near-surface

chlorophyll, J. Geophys. Res.-Oceans, 119, 8195–8220, https://doi.org/10.1002/2014JC010111, 2014.

Gaube, P., Chelton, D. B., Samelson, R. M., Schlax, M. G., and O'Neill, L. W.: Satellite observations of mesoscale eddy-Induced Ekman pumping, J. Phys. Oceanogr., 45, 104–132, https://doi.org/10.1175/jpo-d-14-0032.1, 2015.

Greaser, S. R., Subrahmanyam, B., Trott, C. B., and Roman-Stork, H. L.: Interactions between mesoscale eddies and synoptic oscillations in the Bay of Bengal during the strong monsoon of 2019, J. Geophys. Res.-Oceans, 125, e2020JC016772, https://doi.org/10.1029/2020JC016772, 2020.

Gulakaram, V. S., Vissa, N. K., and Bhaskaran, P. K.: Characteristics and vertical structure of oceanic mesoscale eddies in the Bay of Bengal, Dynam. Atmos. Oceans, 89, 101131, https://doi.org/10.1016/j.dynatmoce.2020.101131, 2020.

Haëntjens, N., Della Penna, A., Briggs, N., Karp-Boss, L., Gaube, P., Claustre, H., and Boss, E.: Detecting mesopelagic organisms using biogeochemical-Argo floats, Geophys. Res. Lett., 47, e2019GL086088, https://doi.org/10.1029/2019GL086088, 2020.

Ham, Y. G., Kim, J. H., and Luo, J. J.: Deep learning for multi-year ENSO forecasts, Nature, 573, 568–572, https://doi.org/10.1038/s41586-019-1559-7, 2019.

Holte, J. and Talley, L.: A New Algorithm for Finding Mixed Layer Depths with Applications to Argo Data and Subantarctic Mode Water Formation, J. Atmos. Ocean. Tech., 26, 1920–1939, https://doi.org/10.1175/2009jtecho543.1, 2009.

Hsu, P.-C., Lin, C.-C., Huang, S.-J., and Ho, C.-R.: Effects of Cold Eddy on Kuroshio Meander and Its Surface Properties, East of Taiwan, IEEE J. Sel. Top. Appl., 9, 5055–5063, https://doi.org/10.1109/jstars.2016.2524698, 2016.

Jiang, H., Song, Y., Mironov, A., Yang, Z., Xu, Y., and Liu, J.: Accurate mean wave period from SWIM instrument on-board CFOSAT, Remote Sens. Environ., 280, 113149, https://doi.org/10.1016/j.rse.2022.113149, 2022.

Karstensen, J., Schütte, F., Pietri, A., Krahmann, G., Fiedler, B., Grundle, D., Hauss, H., Körtzinger, A., Löscher, C. R., Testor, P., Vieira, N., and Visbeck, M.: Upwelling and isolation in oxygen-depleted anticyclonic modewater eddies and implications for nitrate cycling, Biogeosciences, 14, 2167–2181, https://doi.org/10.5194/bg-14-2167-2017, 2017.

Klemas, V. and Yan, X.-H.: Subsurface and deeper ocean remote sensing from satellites: An overview and new results, Prog. Oceanogr., 122, 1–9, https://doi.org/10.1016/j.pocean.2013.11.010, 2014.

Kumar, S. P., Madhupratap, M., Kumar, M. D., Muraleedharan, P., De Souza, S., Gauns, M., and Sarma, V.: High biological productivity in the central Arabian Sea during the summer monsoon driven by Ekman pumping and lateral advection, Curr. Sci. India, 81, 1633–1638, 2001.

Kumar, S. P., Muraleedharan, P. M., Prasad, T. G., Gauns, M., Ramaiah, N., de Souza, S. N., Sardesai, S., and Madhupratap, M.: Why is the Bay of Bengal less productive during summer monsoon compared to the Arabian Sea?, Geophys. Res. Lett., 29, 88-1–88-4, https://doi.org/10.1029/2002gl016013, 2002.

Lecun, Y., Bengio, Y., and Hinton, G. E.: Deep learning, Nature, 521, 436–444, https://doi.org/10.1038/nature14539, 2015.

Ledwell, J. R., McGillicuddy Jr., D. J., and Anderson, L. A.: Nutrient flux into an intense deep chlorophyll layer in a mode-water eddy, Deep-Sea Res. Pt. II, 55, 1139–1160, 2008.

Lee, C. M., Jones, B. H., Brink, K. H., and Fischer, A. S.: The upper-ocean response to monsoonal forcing in the Arabian Sea: seasonal and spatial variability, Deep-Sea Res. Pt. II, 47, 1177–1226, 2000.

Lehahn, Y., d'Ovidio, F., Levy, M., Amitai, Y., and Heifetz, E.: Long range transport of a quasi isolated chlorophyll patch by an Agulhas ring, Geophys. Res. Lett., 38, L16610, https://doi.org/10.1029/2011gl048588, 2011.

Liu, Y., Chen, G., Sun, M., Liu, S., and Tian, F.: A parallel SLA-based algorithm for global mesoscale eddy identification, J. Atmos. Ocean. Tech., 33, 2743–2754, https://doi.org/10.1175/JTECH-D-16-0033.1, 2016.

Liu, Y. and Li, X.: A deep learning-based surface- and subsurface-intensified eddy detection model, figshare [data set], https://doi.org/10.6084/m9.figshare.23599473, 2023a.

Liu, Y. and Li, X.: Eddy-induced Chlorophyll-a Variations in the Northern Indian Ocean, figshare [code], https://doi.org/10.6084/m9.figshare.23599683, 2023b.

Lu, W., Su, H., Yang, X., and Yan, X.-H.: Subsurface temperature estimation from remote sensing data using a clustering-neural network method, Remote Sens. Environ., 229, 213–222, https://doi.org/10.1016/j.rse.2019.04.009, 2019.

Maritorena, S., d'Andon, O. H. F., Mangin, A., and Siegel, D. A.: Merged satellite ocean color data products using a bio-optical model: Characteristics, benefits and issues, Remote Sens. Environ., 114, 1791–1804, https://doi.org/10.1016/j.rse.2010.04.002, 2010.

Mcdougall, T. J. and Barker, P. M.: Getting started with TEOS-10 and the Gibbs Seawater (GSW) Oceanographic Toolbox, SCOR/IAPSO WG, 127, 1–28, 2011.

McGillicuddy Jr., D. J.: Formation of Intrathermocline Lenses by Eddy-Wind Interaction, J. Phys. Oceanogr., 45, 606–612, https://doi.org/10.1175/jpo-d-14-0221.1, 2015.

McGillicuddy Jr., D. J., Anderson, L. A., Bates, N. R., Bibby, T., Buesseler, K. O., Carlson, C. A., Davis, C. S., Ewart, C., Falkowski, P. G., and Goldthwait, S. A.: Eddy/wind interactions stimulate extraordinary mid-ocean plankton blooms, Science, 316, 1021–1026, 2007.

Meunier, T., Tenreiro, M., Pallàs-Sanz, E., Ochoa, J., Ruiz-Angulo, A., Portela, E., Cusí, S., Damien, P., and Carton, X.: Intrathermocline eddies embedded within an anticyclonic vortex ring, Geophys. Res. Lett., 45, 7624–7633, https://doi.org/10.1029/2018GL077527, 2018.

Mignot, A., Claustre, H., Uitz, J., Poteau, A., d'Ortenzio, F., and Xing, X.: Understanding the seasonal dynamics of phytoplankton biomass and the deep chlorophyll maximum in oligotrophic environments: A Bio-Argo float investigation, Global Biogeochem. Cy., 28, 856–876, https://doi.org/10.1002/2013GB004781, 2014.

Paillet, J., Le Cann, B., Carton, X., Morel, Y., and Serpette, A.: Dynamics and evolution of a northern meddy, J. Phys. Oceanogr., 32, 55–79, 2002.

Piontkovski, S., Al-Azri, A., and Al-Hashmi, K.: Seasonal and interannual variability of chlorophyll *a* in the Gulf of Oman compared to the open Arabian Sea regions, Int. J. Remote Sens., 32, 7703–7715, https://doi.org/10.1080/01431161.2010.527393, 2011.

Prasad, T. G.: A comparison of mixed-layer dynamics between the Arabian Sea and Bay of Bengal: One-dimensional

model results, J. Geophys. Res.-Oceans, 109, C03035, https://doi.org/10.1029/2003jc002000, 2004.

Pujol, M.-I., Faugère, Y., Taburet, G., Dupuy, S., Pelloquin, C., Ablain, M., and Picot, N.: DUACS DT2014: the new multi-mission altimeter data set reprocessed over 20 years, Ocean Sci., 12, 1067–1090, https://doi.org/10.5194/os-12-1067-2016, 2016.

Reynolds, R. W., Smith, T. M., Liu, C., Chelton, D. B., Casey, K. S., and Schlax, M. G.: Daily high-resolution-blended analyses for sea surface temperature, J. Climate, 20, 5473–5496, https://doi.org/10.1175/2007JCLI1824.1, 2007.

Roesler, C., Uitz, J., Claustre, H., Boss, E., Xing, X., Organelli, E., Briggs, N., Bricaud, A., Schmechtig, C., and Poteau, A.: Recommendations for obtaining unbiased chlorophyll estimates from in situ chlorophyll fluorometers: A global analysis of WET Labs ECO sensors, Limnol. Oceanogr., 15, 572–585, https://doi.org/10.1002/lom3.10185, 2017.

Ronneberger, O., Fischer, P., and Brox, T.: U-Net: Convolutional Networks for Biomedical Image Segmentation, Cham, Springer International Publishing, 234–241, https://doi.org/10.48550/arXiv.1505.04597, 2015.

Shafeeque, M., Balchand, A. N., Shah, P., George, G., B. R, S., Varghese, E., Joseph, A. K., Sathyendranath, S., and Platt, T.: Spatio-temporal variability of chlorophyll *a* in response to coastal upwelling and mesoscale eddies in the South Eastern Arabian Sea, Int. J. Remote Sens., 42, 4836–4863, https://doi.org/10.1080/01431161.2021.1899329, 2021.

Siegel, D. A., Peterson, P., McGillicuddy, D. J., Maritorena, S., and Nelson, N. B.: Bio-optical footprints created by mesoscale eddies in the Sargasso Sea, Geophys. Res. Lett., 38, L13608, https://doi.org/10.1029/2011gl047660, 2011.

Smitha, B., Sanjeevan, V., Padmakumar, K., Hussain, M. S., Salini, T., and Lix, J.: Role of mesoscale eddies in the sustenance of high biological productivity in North Eastern Arabian Sea during the winter-spring transition period, Sci. Total Environ., 809, 151173, https://doi.org/10.1016/j.scitotenv.2021.151173, 2022.

Somayajulu, Y. K., Murty, V. S. N., and Sarma, Y. V. B.: Seasonal and inter-annual variability of surface circulation in the Bay of Bengal from TOPEX/Poseidon altimetry, Deep-Sea Res. Pt. II, 50, 867–880, https://doi.org/10.1016/S0967-0645(02)00610-0, 2003.

Su, H., Wu, X., Yan, X.-H., and Kidwell, A.: Estimation of subsurface temperature anomaly in the Indian Ocean during recent global surface warming hiatus from satellite measurements: A support vector machine approach, Remote Sens. Environ., 160, 63–71, https://doi.org/10.1016/j.rse.2015.01.001, 2015.

Su, H., Zhang, T., Lin, M., Lu, W., and Yan, X.-H.: Predicting subsurface thermohaline structure from remote sensing data based on long short-term memory neural networks, Remote Sens. Environ., 260, 112465, https://doi.org/10.1016/j.rse.2021.112465, 2021.

Su, J., Strutton, P. G., and Schallenberg, C.: The subsurface biological structure of Southern Ocean eddies revealed by BGC-Argo floats, J. Marine Syst., 220, 103569, https://doi.org/10.1016/j.jmarsys.2021.103569, 2021.

Sun, B., Liu, C., and Wang, F.: Global meridional eddy heat transport inferred from Argo and altimetry observations, Sci. Rep.-UK, 9, 1345, https://doi.org/10.1038/s41598-018-38069-2, 2019.

Thomas, L. N.: Formation of intrathermocline eddies at ocean fronts by wind-driven destruction of potential vorticity, Dynam. Atmos. Oceans, 45, 252–273, https://doi.org/10.1016/j.dynatmoce.2008.02.002, 2008.

Trott, C. B., Subrahmanyam, B., Chaigneau, A., and Delcroix, T.: Eddy tracking in the northwestern Indian Ocean during southwest monsoon regimes, Geophys. Res. Lett., 45, 6594–6603, https://doi.org/10.1029/2018gl078381, 2018.

Trott, C. B., Subrahmanyam, B., Chaigneau, A., and Roman-Stork, H. L.: Eddy-induced temperature and salinity variability in the Arabian Sea, Geophys. Res. Lett., 46, 2734–2742, https://doi.org/10.1029/2018GL081605, 2019.

Wang, Z.-F., Sun, L., Li, Q.-Y., and Cheng, H.: Two typical merging events of oceanic mesoscale anticyclonic eddies, Ocean Sci., 15, 1545–1559, https://doi.org/10.5194/os-15-1545-2019, 2019.

Yang, G., Wang, F., Li, Y., and Lin, P.: Mesoscale eddies in the northwestern subtropical Pacific Ocean: Statistical characteristics and three-dimensional structures, J. Geophys. Res.-Oceans, 118, 1906–1925, https://doi.org/10.1002/jgrc.20164, 2013.

Yang, X., Xu, G., Liu, Y., Sun, W., Xia, C., and Dong, C.: Multi-Source Data Analysis of Mesoscale Eddies and Their Effects on Surface Chlorophyll in the Bay of Bengal, Remote Sens.-Basel, 12, 3485, https://doi.org/10.3390/rs12213485, 2020.

Zhan, P., Guo, D., and Hoteit, I.: Eddy-induced transport and kinetic energy budget in the Arabian Sea, Geophys. Res. Lett., 47, e2020GL090490, https://doi.org/10.1029/2020GL090490, 2020.

Zhang, Z., Qiu, B., Klein, P., and Travis, S.: The influence of geostrophic strain on oceanic ageostrophic motion and surface chlorophyll, Nat. Commun., 10, 2838, https://doi.org/10.1038/s41467-019-10883-w, 2019.